metals

MDPI

Article

Acoustic Emission During Rubber-like Deformation in $Ni_{51}Fe_{18}Ga_{27}Co_4$ Single Crystalline Shape Memory Alloys

Lajos Daróczi [1], Sarah M. Kamel [1,2], László Z. Tóth [1], Elena Yu. Panchenko [3], Yuri I. Chumljakov [3] and Dezső L. Beke [1,*]

[1] Department of Solid State Physics, Doctoral School of Physics, Faculty of Science and Technology, University of Debrecen, P.O. Box 400, 4002 Debrecen, Hungary; lajos.daroczi@science.unideb.hu (L.D.); sarahkamel@science.unideb.hu (S.M.K.); toth.laszlo@science.unideb.hu (L.Z.T.)
[2] Physics Department, Faculty of Science, Ain Shams University, Abbassia, Cairo 11566, Egypt
[3] Siberian Physical Technical Institute, Tomsk State University, Tomsk 634050, Russia; panchenko@mail.tsu.ru (E.Y.P.); chum@phys.tsu.ru (Y.I.C.)
* Correspondence: dbeke@science.unideb.hu

Abstract: Acoustic emission, AE, belonging to a rubber-like deformation in a martensitic state after the stabilization aging of the stress-induced martensite (SIM aging) of $Ni_{51}Fe_{18}Ga_{27}Co_4$ single crystals in compression, were investigated. AE activity in the plateau regions of the stress–strain loop is due to a massive reorientation from the variants produced by SIM aging to the variants preferred by the compressive stress (perpendicular to the stress used in SIM aging) and vice versa. For unloading, the large AE activity just at the knee point of the stress–stain curve is attributed to the difficulty of the re-nucleation of the SIM aging-stabilized martensite variant. The amplitude, peak energy, and area of signals can be described by power-like distributions and the characteristic exponents are in good agreement with data obtained in other alloys. Power law cross-correlations between the energy, E, and amplitude, A, as well as between the area, S, and the amplitude, A, were also analyzed. It was found that the exponents are given by $3-\varphi$ as well as $2-\varphi$, respectively, with $\varphi \cong 0.7$. Normalized universal temporal shapes of avalanches (i.e., the $\frac{U}{A}$ versus $\frac{t}{A^{1-\varphi}}$ plots, where U is the detected voltage) for a fixed area scale very well together. The tail of the normalized temporal shape decays more slowly than the theoretical prediction, which can be attributed to an intrinsic absorption of AE signals and/or to the overlap of sub-avalanches.

Keywords: rubberlike effect; martensite stabilization; acoustic emission; noise analysis

Academic Editor: Gang Fang

Received: 23 December 2024
Revised: 22 January 2025
Accepted: 25 January 2025
Published: 28 January 2025

Citation: Daróczi, L.; Kamel, S.M.; Tóth, L.Z.; Panchenko, E.Y.; Chumljakov, Y.I.; Beke, D.L. Acoustic Emission During Rubber-like Deformation in $Ni_{51}Fe_{18}Ga_{27}Co_4$ Single Crystalline Shape Memory Alloys. *Metals* **2025**, *15*, 131. https://doi.org/10.3390/met15020131

1. Introduction

The deformation of shape memory materials in a martensitic state can result in a large residual strain due to the rearrangement of martensite variants (a superplastic behavior) into a single variant structure preferred by the applied stress [1]. Aging in a martensitic state under uniaxial stress (also called the stabilization aging of stress-induced martensite or SIM aging) [2–10] leads to a stabilization of the induced martensite variant and its reorientation (under a stress perpendicular to the direction applied during SIM aging) and shows a hysteresis on the stress–strain curve without a significant residual strain (rubber-like behavior) [2]. Thus, this rubber-like behavior, compatible with the two-way shape memory recoverable strain of the usual shape memory alloys can have important practical applications due to the large reversible shape change induced either by the uniaxial stress or magnetic field in ferromagnetic shape memory alloys [6–10]. The most

important mechanism of the variant rearrangement is the twin boundary motion, which has a discontinuous character, leading to acoustic emission, AE, signals [11–14].

The above intermittent character is manifested in the emission of signal avalanches, which have characteristic statistical behavior. The probability distribution density function of a typical signal parameter, x (like the peak amplitude, A, area, S, or energy, E), according to the tuned criticality behavior [15], follows a truncated power law form [12,15]:

$$P(x) \propto x^{-\mu} \exp\left(-\frac{x}{x_c}\right) \quad (1)$$

where μ is the characteristic exponent and x_c is the cutoff value. Here, x denotes a measured parameter of the avalanche, like the amplitude, A, area, S, or energy, E, or duration, D. Furthermore, well-known power law relations exist between the measured avalanche parameters and, e.g., the mean field theory, MFT, [15–17] predicts that $S \sim D^{\gamma}$ with $\gamma = 2$ and $S \propto A^2$, $E \propto A^3$. Such power relations are consequences of the self-similarity of the crackling noises [15].

It is well known that due to experimental difficulties (finite threshold values [18,19] and transfer distortions of the original source signal [18–20]), most of the measured parameters cannot reflect the features of the source (i.e., the rate of the intermittent local shape changes during twin reorientations). For example, the duration time, D, (and related parameters containing D in their definitions) for AE avalanches can be strongly polluted by the internal absorption of the AE waves (which can be characterized by an exponential expression, $e^{-\frac{t}{\tau_a}}$, where τ_a is the attenuation time) [18,19]. It was shown in [19] that, although the exponents of the probability distribution functions can be more or less free of such effects, the scaling relations between the measured parameters can be strongly influenced. Moreover, it was also pointed out in [19] that the correlations between S and A as well as E and A can be characterized by exponents considerably less than the values given by the MFT. This is called "enigma" for acoustic emission [19]. In a recent communication [18], the above enigma was investigated by assuming a power relation between A and the rising time, R, of the AE signal ($R \propto A^{1-\varphi}$), and it was found that $S \propto A^{2-\varphi}$ and $E \propto A^{3-\varphi}$ holds, respectively. The values of φ were the same for the intermittent motions of interfaces between martensite and austenite in two different shape memory single crystals, (of $Ni_{45}Co_5Mn_{36.6}In_{13.4}$ and $Ni_{49}Fe_{18}Ga_{27}Co_6$ alloys) with $\varphi = 0.8 \pm 0.2$ for both alloys.

It is also well known that the above-mentioned exponents in Equation (1) are quite robust, and change only slightly for different mechanisms [18,21]. Thus, the focus is increasingly on the average temporal shapes of avalanches, i.e., the average of the detected voltage signal ($U(t)$) of the magnetic or acoustic emission for the fixed size or duration [16,17,20,22], which can be better related to the given type of the mechanism [16,17]. Regarding the average avalanche shape for fixed area, S, it was obtained from the theory [22] that

$$U(t) \sim < v(T) >_S = ate^{-\left(\frac{t}{\tau}\right)^2} \quad (2)$$

where $v(T)$ and $U(t)$ are the interface velocity and the detected voltage. a and τ are non-universal (material-dependent) constants: τ is the characteristic time of the avalanche decay [23]. On this basis, the self-similarity of the emitted avalanches [21] is expected, and using appropriate scaling parameters, the normalized $U(t)$ functions should fall on a common curve for different bins of S. For the experimental verification, whether an appropriate scaling can indeed lead to good scaling together, dividing both axes by $S^{0.5}$ (based on the power relations predicted by MFT, i.e., $A \propto S^{0.5}$ as well as $D \propto A$) was used [20,23,24]. However, no good scaling was achieved, and the curves did not scale completely in a universal way. As it was mentioned above, there exists a power relation between A and

R as well, as follows: $R \propto A^{1-\varphi}$ [18]. Thus, by scaling the voltage by A and the time by $A^{1-\varphi}$, nice common functions were obtained not only for the motion of interfaces between austenite and martensite in $Ni_{49}Fe_{18}Ga_{27}Co_6$ single crystals [18], but for the motion of the individual twin boundary (of type I) in Ni-Mn-Ga single crystals [25] too.

This paper, we present experimental results on AE measurements during rubber-like deformation (i.e., during twin rearrangements) of $Ni_{51}Fe_{18}Ga_{27}Co_4$ ferromagnetic shape memory single crystals. According to the best of our knowledge, this is the first complete AE investigation for the whole cycle of such a large (about 15%) rubber-like recoverable strain. In addition to the determination of the characteristic exponents in Equation (1), the scaling relations between the area and peak amplitude as well as between the energy and peak amplitude are determined and the obtained power exponents of these are used to find normalization factors for the construction of universal average temporal avalanche shapes. Our results will also be compared with AE results obtained during the stress- or magnetic field-induced motion of single twin boundaries or different ensembles of twin boundaries in Ni_2MnGa alloys. Universal averaged temporal avalanches are also constructed at a fixed area, by dividing the voltage and time scales by A as well as by $A^{1-\varphi}$, using the φ value calculated from the exponents of power relations between the S and A as well as between the E and A.

2. Experimental

The $Ni_{51}Fe_{18}Ga_{27}Co_4$ single crystals were prepared using vacuum induction melting and the single crystals were grown by the Bridgman method in a helium atmosphere at Tomsk University, Russia. Dimensions of the sample were $3 \times 3 \times 5$ mm. Homogenization heat treatment was performed at 1175 °C for 1 h, which was followed by a quench to room temperature. The B2 high-temperature phase of the quenched crystals undergoes a martensitic transformation to the L10-martensite. SIM (stress-induced martensite) stabilization aging was performed under compression along the $[110]_A$ direction in the martensitic state at 150 °C for 1 h.

Compression tests were made by an Instron 4465 tensile test machine at room temperature along the $[001]_A$ direction. Acoustic emission (AE) measurements were performed by a piezoelectric sensor (MICRO-100S from Physical Acoustic Corporation, Princeton Junction, NJ, USA), attached to the steel compression anvil (Figure 1). The microphone had a good frequency response between 100 KHz and 1 MHz, which is nearly flat in the range between 0.2 and 1 MHz (at about −75 dB in average) with maximum ± 10 dB deviation (1 V reference value). The microphone was integrated with a 30 dB pre-amplifier. Furthermore, we connected a primary amplifier to the microphone with logarithmic gain, offering a dynamic range of 90 dB and operating within a band pass frequency range of 30 KHz to 1 MHz. For the conditioning and acquisition of acoustic data, a Sensophone (Geréb and Co GmbH, Budapest, Hungary) AE measurement system was used with a 8 MS/s sampling rate (for the details, see [26]). In the evaluation of acoustic signals, a 0.04 V threshold value and a 4×10^{-5} s hit detection time was used.

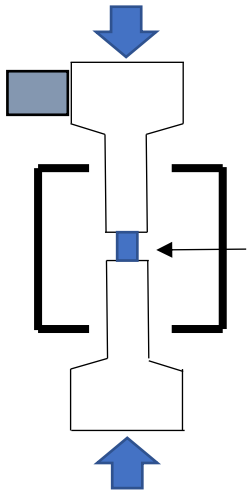

Figure 1. Schematic picture of the measuring setup. The arrow shows the sample and the box at the top anvil is the sensor.

3. Results

The stress–strain curve, taken with a strain rate of 1.25 × 10−3 s−1 along the $[001]_A$ direction (which is perpendicular to the $[110]_A$ direction of SIM aging) during the rubber-like behavior of the $Ni_{51}Fe_{18}Ga_{27}Co_4$ sample, is presented in Figure 2a. The cycles were stable and curves of more than 10 cycles were fully collapsed. As the result of SIM aging (see, e.g., [7]), the recoverable strain is around 15%. Figure 2b shows the stress curves, and the simultaneously measured AE signals as well as the cumulative energy of the AE signals ($\sum \boldsymbol{E} = \boldsymbol{E_i}$) as the function of time. The number of AE events remarkably increases on the unloading curve (at around 125 s on Figure 2b), with a large jump in $\sum \boldsymbol{E}$.

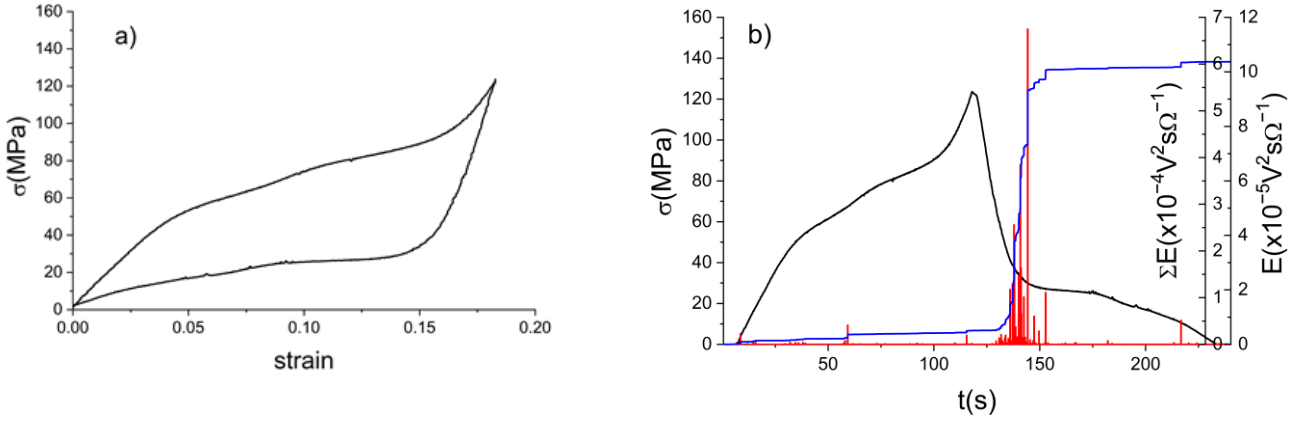

Figure 2. (**a**) Compression stress–strain curve; (**b**) stress (black), energy of acoustic emission signals (red), and the cumulative AE energy, $\sum \boldsymbol{E}$, (blue) as a function of time (taken with a 1.25 × 10^{-3} s^{-1} strain rate). A large acoustic activity and large jump in $\sum \boldsymbol{E}$ can be observed on the unloading curve.

The AE data were used for the calculation of the characteristic exponents in Equation (1) for the area, *S*, energy, *E*, and amplitude, *A*. The *S*, *E*, and *A* of acoustic avalanches were calculated from the detected voltage, $\boldsymbol{U(t)}$ (temporal avalanche shape) according to their usual definitions [25]: *A* is the maximum value, $\boldsymbol{S} = \int_0^D \boldsymbol{U}(\boldsymbol{t})\boldsymbol{dt}$, and $\boldsymbol{E} = \frac{1}{R_o}\int_0^D \boldsymbol{U}^2(\boldsymbol{t})\boldsymbol{dt}$, where $\boldsymbol{R_o}$ is an arbitrarily chosen resistance ($\boldsymbol{R_o}$ = 1 MΩ).

In order to get the exponents from Equation (1), the probability density functions, PDF, (calculated using a logarithmic boxing of the quantities $\boldsymbol{P(x_i)} \sim \frac{N_i}{N}$, where $\boldsymbol{N_i}$ and $\boldsymbol{N}$ denote the number of events at a certain value of $\boldsymbol{x_i}$ and the number of all hits, respectively) were fitted using a two-parametrical nonlinear fitting by the Levenberg–Marquardt least squares

method. As an illustration, Figure 3 shows the energy probability distribution density of the acoustic signals, averaged for both directions. It can be seen that a straight line can very well fit the points over about four–five orders of magnitude. The maximum likelihood fit is a recommended method to check the reliability of exponents calculated from the log P versus log E plots [27]. We obtained that, in all cases, the exponents determined by the two methods were the same within the error bars given in Table 1 (see also Figure 3a,b). Table 1 shows the calculated exponents for energy, amplitude, and area. We have carried out a sensitivity analysis (always considering the corresponding maximum likelihood fits as well), regarding the small upward curvature in Figure 3a. This is sensitive to the choice of the threshold. The plot shown is the optimum fit with a 0.04 V threshold value.

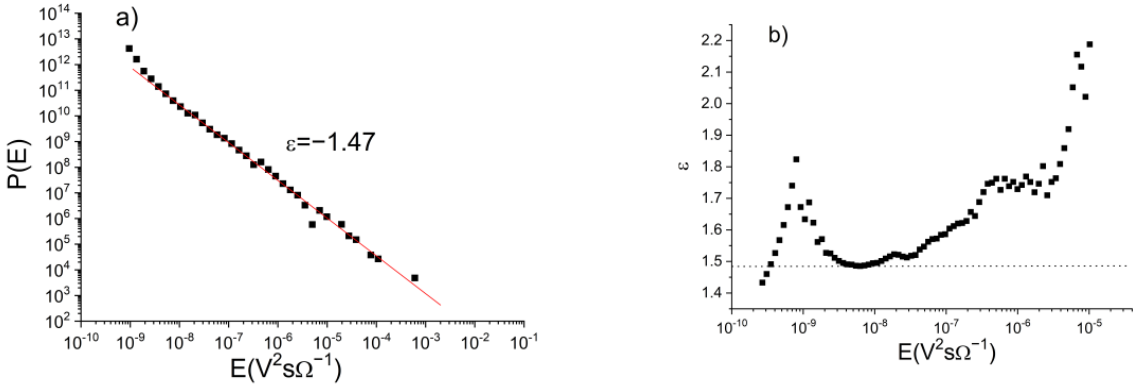

Figure 3. The energy probability distribution density function of acoustic signals obtained during rubber-like deformation (**a**). (**b**) The maximum likelihood fit for the exponent.

Table 1. Power exponents of the acoustic emission parameters.

$P(E) \sim E^{-\varepsilon}$	$P(A) \sim A^{-\alpha}$	$P(S) \sim S^{-\delta}$	$E \sim A^{3-\varphi}$	$S \sim A^{2-\varphi}$
ε	α	δ	φ	φ
1.5 ± 0.1	2.3 ± 0.2	1.6 ± 0.1	0.7 ± 0.1	0.7 ± 0.1

Figures 4 and 5 show the power relations between the energy and amplitude as well as the area and amplitude, respectively. It can be seen that, in addition to the first parts, belonging to small amplitudes, where the amplitude is comparable to the threshold (0.04 V) and a downward curvature is observed (see also Figure 6 and Figure 7 in [18] or Figure 2d in [25]), a straight line can be fitted. As it was shown in [26], such curvature appears if the amplitude per threshold ratio is less than 10. Using the prediction of [18], the exponentsfor the power relations between E and A as well as S and A can be expressed as $\mathbf{3} - \boldsymbol{\varphi}$ as well as $\mathbf{2} - \boldsymbol{\varphi}$, respectively. Table 2 also contains the values of φ obtained from our measurements.

It is worth mentioning that the data collected during the forward and reverse deformation were collapsed into one file; thus, the above exponents were calculated using all (up and down) of the points. This is in contrast to the results obtained from austenite/martensite transformations in different shape memory alloys, where frequently the exponents for the up and down processes were different [28]. We will turn to this below, commenting on the difference of the total numbers ($\sum N = \sum_i N_i$) and total AE energy ($\sum E = \sum_i E_i$) during loading and unloading branches and we will discuss the fine details of the obtained AE data.

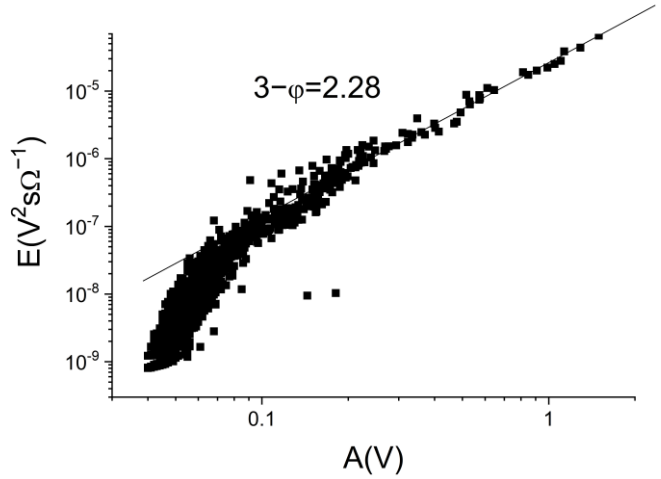

Figure 4. *LogE* versus *LogA*. The insert shows the slope of the straight line fitted.

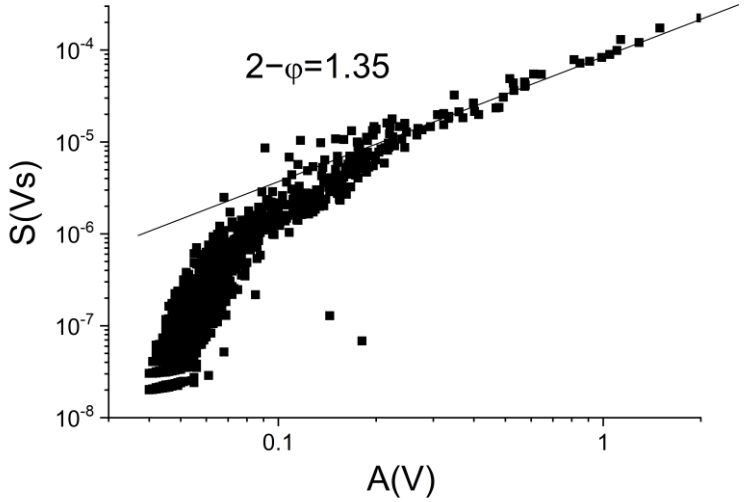

Figure 5. *LogS* versus *LogA*. The insert shows the slope of the straight line fitted.

4. Discussion

4.1. AE During Loading and Unloading

The origin of the rubber-like behavior is the so-called symmetry conforming short-range ordering [29] during SIM aging (which leads to a diffusional stabilization of the given single variant martensite, preferred by applied stress). It is not surprising that the recoverable strain is large for our $Ni_{51}Fe_{18}Ga_{27}Co_4$ single crystals since, in this case, the stabilized martensite structure is dominantly a single martensite variant, and the aging temperature and time of SIM aging was high enough to reach the complete short-range order according to this martensite structure [7]. The single variant martensite reorients during the application of the compressive uniaxial stress (in $[001]_A$ direction, perpendicular to the $[110]_A$ SIM aging direction of austenite) and if it is a complete reorientation then a recoverable strain close to the theoretical value can be reached, which is about 16.6% in this alloy [7]. In our case, the experimental value is about 15% (see Figure 2a), which indicates that the full potential of the transformation strain was not realized in our experiment. This can be related to the fact that the SIM-aged state or the reoriented state (or both) is not a fully de-twinned structure of the corresponding martensite (see also Figure 5). Here, we use the notations of [7] and [30] for this alloy: the dominant variant V1 ($[001]_A$ | | $[001]_M$) is formed during SIM aging, while V2 ($[010]_A$ | | $[001]_M$) and V3 ($[100]_A$ | | $[001]_M$) are the reoriented variants [30] (preferred by the stress under which the rubber-like behavior is

investigated. see also Figure 3a in [7], as well as Figure 2 in [30]) The presence of variants V2 and V3 is the indication of the incomplete de-twinning [30]. Nevertheless, during loading reorientation from the (initially dominant) V1 to V2/V3, it takes place and the reveres process sets in during unloading.

It can be seen from Figure 2 that, for loading, there are some AE signals already before the start of the plateau (at about 3.5% strain), but these most probably can be attributed to micro-friction in the course of matching the sample to the testing machine [31]. The sporadic AE activity and a slight gradual increase of the cumulative AE energy in the whole remaining part of the loading stress–strain/time curve belongs to the reorientation process from V1 to V2/V3. For the unloading part, the situation is different in the sense that here, a large number of AE signals and a large jump in $\sum \boldsymbol{E}$ appear at the beginning of the plateau (at around 125 s), which is followed by a similar lower activity (like along the loading branch) until the end. In this latter plateau region, a jerky rearrangement of the variant structure takes place, either by the nucleation of the V2/V3 variant or by the motion of the already existing boundaries between the V1 and V2/V3 boundaries. The above picture is also in a good qualitative agreement with the simulation results on dynamical tweed, mobile kinks, and movement in the twin walls in ferroelastic materials [32,33]. The amplitude of jumps was higher in the yield regime during nucleation (at around the beginning of the plateau in our case) as compared to the plateau region where the transition between V1 and V2/V3 took place.

The high local activity on the unloading curve also leads to a remarkable difference in the total number of acoustic events and in the total acoustic energy ($\sum_i \boldsymbol{N_i} = 1250$ and 2500 as well as $\sum_i \boldsymbol{E_i}$ =0.5 × 10^{-4} V^2s and 5.5 × 10^{-4} V^2s for loading and unloading, respectively), which suggests that there is an AE asymmetry. Since the nucleation processes typically provide high AE activity [23,32,33], we interpret the asymmetry and large local AE activity on the unloading branch by the difficulty of the re-nucleation of the initial, differently oriented martensite variant V1. The difficulty is related to the almost completely de-twinned structure of the initial state: from the twinned state (Figure 6b) (in which twinning is the manifestation of some local stress relaxations by the formation of twins), the formation of the stabilized de-twinned structure needs to overcome an energy barrier of an elastic origin. Furthermore, the remaining part reflects similarly for the loading branch, with the jerky propagation of the boundaries between the two variants. The relatively large dissipation (wide hysteresis loop in Figure 2a) can also be a fingerprint of the difficult re-nucleation of the V1 variant.

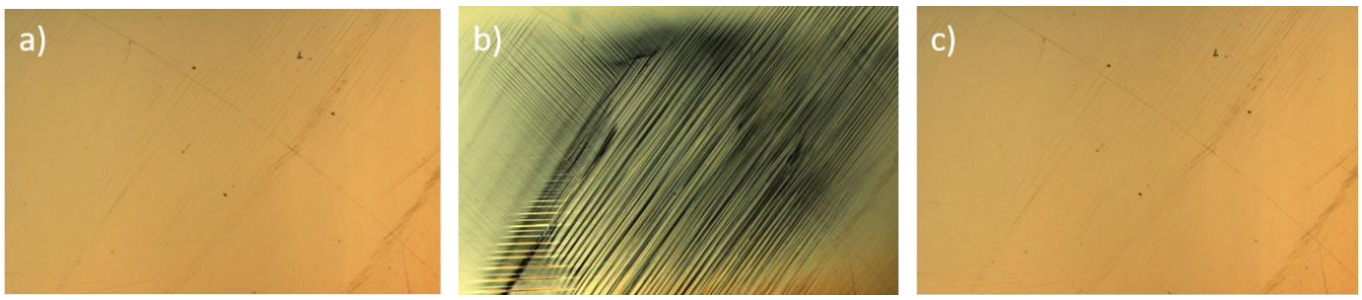

Figure 6. An optical micrograph of the martensite structure: (**a**) original, V1, state with a dominantly de-twinned region, with minor residual twins; (**b**) twinned, reoriented, V2/V3, martensite; and (**c**) the final state, which is equivalent to the initial state.

Thus, it seems that while the processes in the plateau are similar in both branches, the above asymmetry is an indication that there are no nucleation difficulties for the appearance/further growth of the V2/V3 variant in loading, but in unloading, the re-nucleation of V1 is difficult. Understanding the structural details of this calls for a detailed

microscopic investigation. Nevertheless, the fact that the observed transformation strain is less than the theoretically predicted value also reflects that the V1 and V2/V3 end states should not be fully de-twinned variants.

The above asymmetry in $\sum \boldsymbol{N}$ and $\sum \boldsymbol{E}$ suggests that it is worth checking whether the exponents of signals collected from the large local activity region only for unloading are the same as the average values given in Table 1 or not. We will turn back to this point below.

4.2. Power Exponents of the Acoustic Emission Parameters

Firstly, we compare the exponents of the amplitude or energy probability density functions, with exponents given in previous publications obtained either from the magnetic field- or stress field-induced martensite variant rearrangements in ferromagnetic shape memory alloys [11,13,25,34–36]. Table 2 contains the summary of the measured exponents, with our value calculated from all of the measured points.

Table 2. Characteristic exponents of the energy (ε) and amplitude (α) distributions measured during the external field-induced rearrangements of martensite variants and/or during the jerky shift of individual twin boundaries.

Single Crystal	Summary	ε	α
$Ni_{51}Fe_{18}Ga_{27}Co_4$, this work, averaged	Rubber-like, Stress-induced	1.5 ± 0.1	2.3 ± 0.2
Ni_2MnGa [13]	Single twin boundary Type I, stress-induced		2.3 ± 0.2
Ni_2MnGa [13]	Single twin boundary Type II, stress-induced (less than one decade energy range)		3.0 ± 0.2
Ni_2MnGa [34]	Type II	1.5 ± 0.1	
Ni_2MnGa [35]	Type I	1.5 ± 0.1	
Ni_2MnGa [25]	Single twin boundary Type I, stress-induced	1.5 ± 0.1	2.1 ± 0.1
Ni_2MnGa [36]	After compression along the [100] direction, magnetic field-induced	1.5 ± 0.1	1.8 ± 0.2

In [13,25,35], the AE results for a type I twin boundary were analyzed in Ni_2MnGa, while in [36], rearrangements of a magnetic field-induced twin boundary network was investigated. In Ni_2MnGa single crystals, the same energy and amplitude exponents can be concluded (if we do not take into account the results of [13] for type II twin boundaries, where less than one order of a magnitude-wide energy range was covered), which can be summarized by $\varepsilon = 1.5 \pm 0.2$ and $\alpha = 2.1 \pm 0.2$, respectively. It can also be seen from Table 2 that our present results are in good agreement with the above average data.

Thus, we can also conclude that the energy and amplitude exponents were the same both for the stress- or magnetic field-induced motion of single boundary or for the motion of different ensembles of twin boundaries in two different ferromagnetic shape memory materials. This result is similar to the conclusion drawn on AE exponents (with slightly different average values as obtained for twin boundary motions) collected during the austenite/martensite transformations in Ni_2MnGa, $Ni_{51}Fe_{18}Ga_{27}Co_4$, and $Ni_{45}Co_5Mn_{36.6}In_{13.4}$ single crystals [26].

The above results nicely demonstrate the robustness of the characteristic exponents present in relations given by Equation (1). It can also be seen that the φ values, as ex-

pected [18,25], are the same as calculated either from the cross-correlation between E and A or S and A.

As it was mentioned already in the introduction, it is worth going beyond the comparison of the energy and amplitude exponents only to investigate the scaling properties of the temporal avalanche shapes at fixed areas. Before this, it is worth checking the exponents of the AE parameters collected after the separation of the AE signals belonging to the large local AE activity during the re-nucleation of the SIM ageing-stabilized variant, V1. We carefully carried out this analysis and found that all the energies given in Table 1 were the same for both the separated and the remaining signals within the error bars. In addition, in Figures 4 and 5, and on the corresponding plots after separation, not any branching was observed. As it has been shown in a series of papers [37–40], the multibranching (i.e., $E = s_i A_i^2$ and for i = 1 and 2, $s_1 \neq s_2$) stems from the overlapping of sub-avalanches within one acoustic emission signal and the extent of this overlap can be different for different avalanche mechanisms. It was also shown that this effect can be very useful in making distinctions between different avalanche mechanisms [37]. Thus, we can conclude that on the basis of our results, no distinction can be made between AE signals belonging to the re-nucleation of the V1 variant and to the massive reorientation of the two variants (in the plateau regions).

4.3. Normalized Temporal Avalanche Shapes for Fixed Duration and Area

The next step is the construction of the normalized (universal) temporal avalanche shapes for a fixed area. The normalized functions for fixed area, in accordance with [18] and [25], can be obtained from (2) by scaling the voltage scale with A and the time scale with $A^{1-\varphi}$, since according to [26] $R \propto A^{\varphi}$ with $\varphi = 0.7$ (see Table 1). In constructing the average avalanche shapes, firstly different avalanche size ranges (bins) were selected. Within each size range, the avalanches were averaged, and the common avalanche parameters (amplitude, size, energy, and rising time) were determined for the average function belonging to this bin (see Figure 7). As a second step these functions were scaled together by dividing the U axis by A and the t axis by $A^{1-\varphi}$, as it is shown in Figure 8. It can be seen that, as expected, the averaged curves are collapsed, showing the self-similarity of the avalanches over a wide size range. It is worth commenting on two characteristics of Figure 8: (a) fluctuations (i.e., only a smoothed curve would fit to the shape predicted from Equation (2)), and (b) the last part (above about a 300 reduced time) decays much more slowly than predicted by Equation (2). The fluctuating behavior can be a consequence of our relatively bad statistics as compared, e.g., with similar AE measurements on motion of individual twin boundary in Ni_2MnGa single crystals (the number of events was about five times larger in [25] than in here). Another possibility is the effect of mechanical oscillations in the otherwise monotonic driving force [41]; if the typical durations of avalanches is comparable to the period of oscillations of the testing machine, some oscillations can appear on the temporal avalanche shape (this effect is expected to be more expressed in experiments made on micro-pillars [41]). However, as compared to our measurements, in $Ni_{49}Fe_{18}Ga_{27}Co_6$ [18], the duration times of avalanches emitted during martensitic transformation covered a similar range and the testing machine was the same: no oscillations were observed on the averaged temporal shapes. Regarding the behavior b), it can be noted that while in [25], the tail of the normalized temporal shapes at fixed area followed Equation (2) ($\sim e^{-\frac{t}{2}^{*2}}$, $t^* = \frac{t}{A^{1-\varphi}}$) with exponent 2, as expected, for Ni_2MnGa [25] or in $Ni_{49}Fe_{18}Ga_{27}Co_6$ [18,25], here, an exponent of about 1 can be obtained (see Figure 9). This latter value is similar to the exponent obtained in [23] where it was mentioned that it can be related to the absorption of the acoustic signals [18,23] characterized by an $\sim e^{-\frac{t}{\tau_a}}$ type function. From such a fit, a $\tau_a \cong 150$ μs attenuation time can be estimated which is in

reasonable agreement with data obtained from AE experiments in $BaTiO_3$ (τ_a = *20* μs) [19]. However, in [23], it was also discussed as a still-open question, that the presence of a slower decay in the tail region can also be related to the contribution of sub-avalanches. This can lead to the Omori-type decay (postseismic slip), observed in earthquakes [42]): $\sim t^{-p}$ with $p \cong 1$. Figure 10 shows the $logU^*$ versus $logt^*$ plot and it can be seen that it can also be fitted with a straight line and the slope of this is $p = 0.91$. Deciding between the above two possible explanations calls for further investigations.

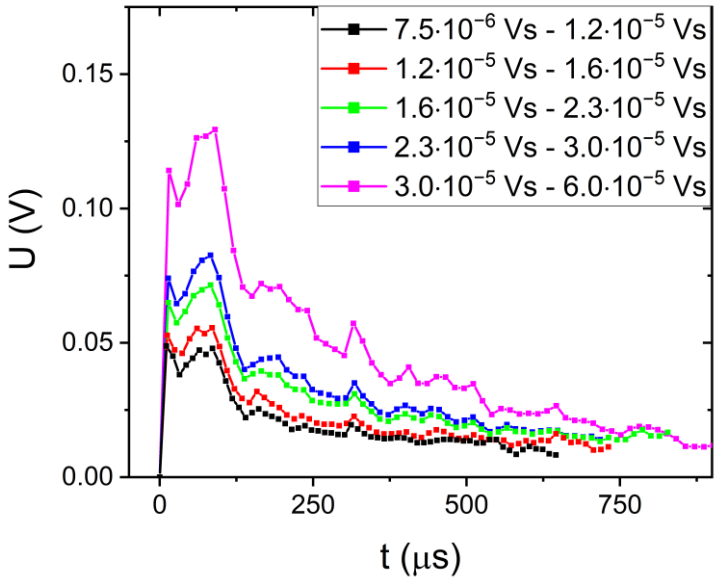

Figure 7. Averaged AE signals in different size (area) ranges (the insert gives the center values of S within which the averaging was made).

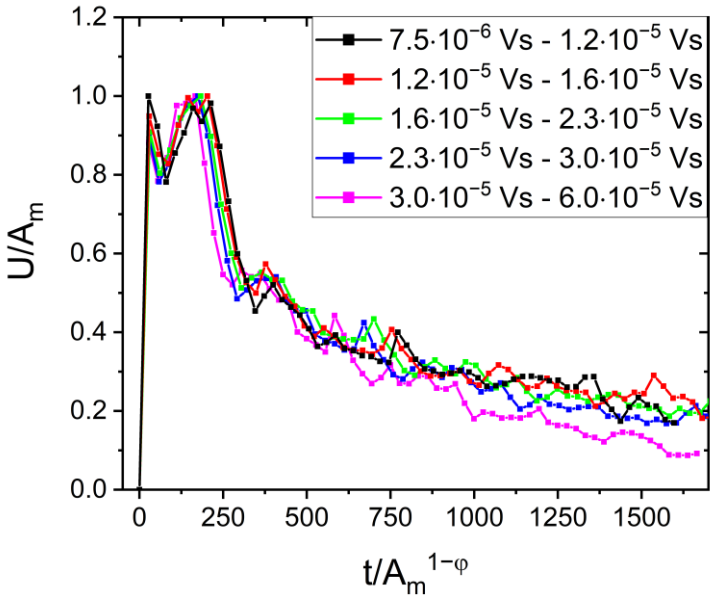

Figure 8. Averaged AE signals after a normalization of the vertical and horizontal axes by A_m and $A_m^{1-\varphi}$, respectively.

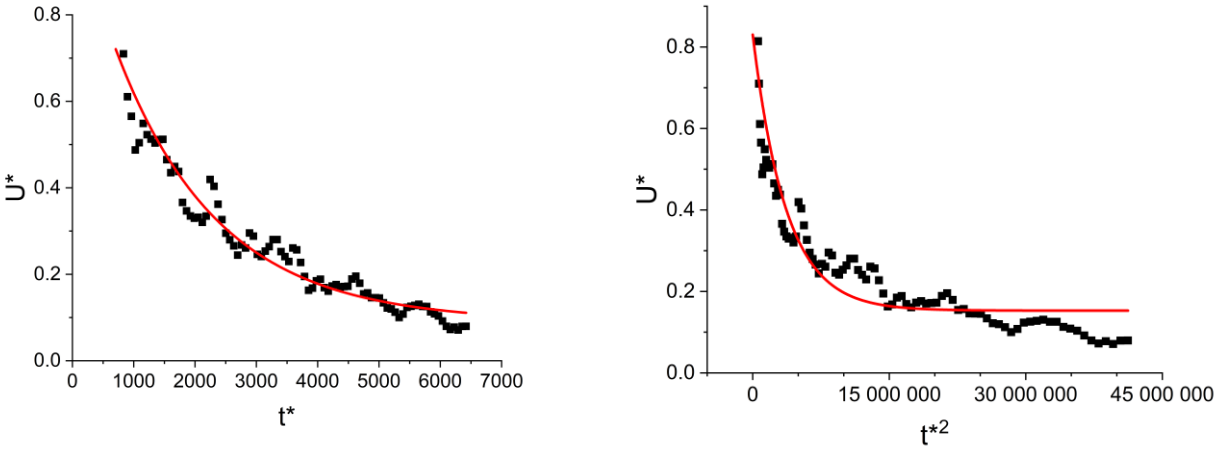

(**a**) (**b**)

Figure 9. Fitting the exponentially decaying tail of the curve on Figure 10 ($U^* = \frac{U}{A}$ and $t^* = \frac{t}{A^{1-\varphi}}$): according to Equation (2) (**a**) as well as by $\sim e^{-\frac{t}{\tau_a}}$ type function (**b**). It can be seen that the fit $\sim e^{-\frac{t}{\tau_a}}$ is better, and it yields $\tau_a \cong 150$ μs.

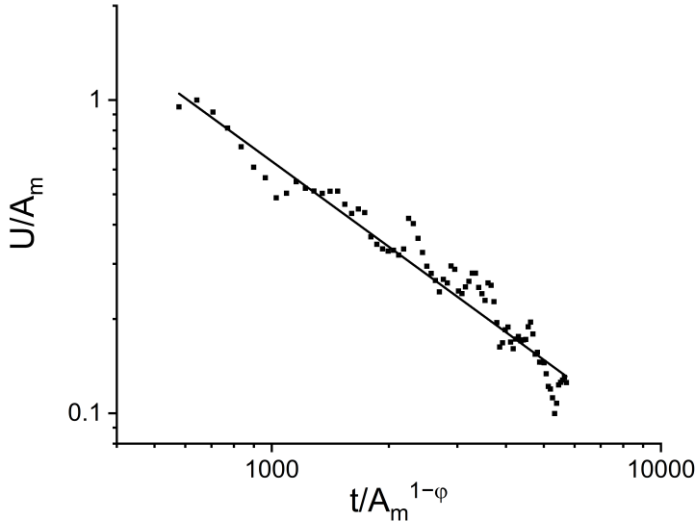

Figure 10. A $logU^*$ versus $logt^*$ plot from the tail region of Figure 8.

5. Conclusions

- It is shown that, after SIM aging, there is a well-detectable acoustic emission activity during the rubber-like deformation (up to about 15%) of $Ni_{51}Fe_{18}Ga_{27}Co_4$ single crystals.
- The observed large AE activity at the beginning of the unloading plateau on the stress–stain curve and the observed large AE asymmetry for loading and unloading is attributed to difficulties in the re-nucleation of the SIM-aged martensite variant.
- The characteristic exponents, calculated either from all of the data points, or from the separation of the two types of AE signals (belonging to re-nucleation of the SIM aged variant as well as to reorientations of the competing variants), are the same within the error bars.
- The normalized universal temporal shapes of the avalanches for a fixed area, using the amplitude, A, and $A^{1-\varphi}$ scaling parameters (i.e., the $\frac{U}{A}$ versus $\frac{t}{A^{1-\varphi}}$ plots), were very well scaled together, with φ values obtained from the $E \sim A^{3-\varphi}$ and $S \sim A^{2-\varphi}$ cross-correlation exponents. The tail of this function decays slower by a smaller exponent than the theoretically predicted one, which can be attributed to either the intrinsic absorption of AE signals and/or the overlap of sub-avalanches.

Author Contributions: Conceptualization, D.L.B. and L.D.; methodology, L.D., E.Y.P., Y.I.C. and S.M.K.; software, L.Z.T.; validation, D.L.B., E.Y.P., Y.I.C., L.D. and L.Z.T.; formal analysis, D.L.B., L.D. and L.Z.T.; investigation, L.D. and S.M.K.; data curation, L.D. and L.Z.T.; writing—original draft preparation, D.L.B. and L.D.; writing—review and editing, D.L.B. and L.D.; visualization, L.D.; supervision, D.L.B. and L.D.; All authors have read and agreed to the published version of the manuscript.

Funding: This research was supported by the Ministry of Science and Higher Education of the Russian Federation, project No FSWM-2024-0007.

Data Availability Statement: The original contributions presented in this study are included in the article. Further inquiries can be directed to the corresponding author.

Conflicts of Interest: The authors declare no conflicts of interest.

References

1. Otsuka, K.; Wayman, C.M. *Shape Memory Materials*; Cambridge University Press: Cambridge, UK, 1999.
2. Ren, X.; Otsuka, K. Origin of rubber-like behaviour in metal alloys. *Nature* **1997**, *389/9*, 579–582. [CrossRef]
3. Alaneme, K.K.; Anaele, J.U.; Okotete, E.A. Martensite aging phenomena in Cu-based alloys: Effects of structural transformation, mechanical and shape memory properties: A critical review. *Sci. Afr.* **2021**, *12*, e00760. [CrossRef]
4. Ryklina, E.; Polyakova, K.; AKonopatsky, A.; Teplyakova, C.; Murygin, S.; Andreev, V.; Poletika, T.; Girsova, S.; Komarov, V.; Piskunova, P. Effect of original structure on aging-induced microstructure and transformation behavior of Ni-rich NiTi alloy using various aging modes. *J. Alloys Comp.* **2025**, *1010*, 177859. [CrossRef]
5. Niendorf, T.; Krooβ, P.; Somsen, C.; Eggeler, G.; Chumlyakov, Y.I.; Maier, H.J. Martensite aging—avenue to new high temperature shape memory alloys. *Acta Mater.* **2015**, *89*, 298–304. [CrossRef]
6. Panchenko, E.; Timofeeva, E.; Eftifeeva, A.; Osipovich, S.; Surikov, N.; Chumlyakov, Y.; Gerstein, G.; Maier, H.J. Giant rubber-like behavior induced by martensite aging in Ni51Fe18Ga27Co4 single crystals. *Scr. Mater.* **2019**, *162*, 387–390. [CrossRef]
7. Panchenko, E.Y.; Timofeeva, E.E.; Chumlyakov, Y.I.; Osipovich, K.S.; Tagiltsev, A.I.; Gerstein, G.; Maier, H.J. Compressive shape memory actuation response of stress-induced martensite aged Ni51Fe18Ga27Co4 single crystals. *Mat. Sci. Eng.* **2019**, *A746*, 448–455. [CrossRef]
8. Morito, H.; Fujita, A.; Oikawa, K.; Ishida, K.; Fukamichi, K.; Kainuma, R. Stress assisted magnetic-field-induced strain in Ni-Fe-Ga-Co ferromagnetic shape memory alloys. *Appl. Phys. Lett.* **2007**, *90*, 062505. [CrossRef]
9. Rajput, G.S.; Vora, J.; Prajapati, P.; Chaudhari, R. Areas of recent developments for shape memory alloy: A review. *Mater. Today Proc.* **2022**, *62*, 7194. [CrossRef]
10. Lauhoff, C.; Reul, A.; Langenkämper, D.; Krooß, P.; Somsen, C.; Gutmann, M.J.; Pedersen, B.; Kireeva, I.V.; Chumlyakov, Y.I.; Eggeler, G.; et al. Effects of aging on the stress-induced martensitic transformation and cyclic superelastic properties in Co-Ni-Ga shape memory alloy single crystals under compression. *Acta Mater.* **2022**, *226*, 117623. [CrossRef]
11. Reul, A.; Lauhoff, C.; Krooß, P.; Somsen, C.; Langenkämper, D.; Gutmann, M.J.; Pedersen, B.; Hofmann, M.; Gan, W.M.; Kireeva, I.; et al. On the impact of nanometric γ' precipitates on the tensile deformation of superelastic Co49Ni21Ga30. *Acta Mater.*. [CrossRef]
12. Bronstein, E.; Tóth, L.Z.; Daróczi, L.; Beke, D.L.; Talmon, R.; Shilo, D. Tracking Twin Boundary Jerky Motion at Nanometer and Microsecond Scales. *Adv. Funct. Mater.* **2021**, *31*, 2106573. [CrossRef]
13. Perevertov, A.; Sevcik, M.; Heczko, O. Correlation between Acoustic Emission and Stress Evolution during Single Twin Boundary Motion in Ni-Mn-Ga Magnetic Shape Memory Single Crystal. *Phys. Status Solidi. RRL* **2022**, *17*, 2200245. [CrossRef]
14. Weidner, A.; Vinogradov, A.; Vollmer, M.; Krooß, P.; Kriegel, M.J.; Klemm, V.; Chumlyakov, Y.; Niendorf, T.; Biermann, H. In situ characterization of the functional degradation of a [0,1] orientedFe–Mn–Al–Ni single crystal under compression using acoustic emission measurements. *Acta Mater.* **2021**, *220*, 11733. [CrossRef]
15. Setna, J.P.; Dahmen, K.A.; Myers, C.R. Crackling noise. *Nature* **2001**, *410*, 242–250. [CrossRef]
16. LeBlanc, M.; Angheluta, L.; Dahmen, K.; Goldenfeld, N. Universal fluctuations and extreme statistics of avalanches near the depinning transition. *Phys. Rev. E* **2013**, *87*, 022126. [CrossRef]
17. Papanikolaou, S.; Bohn, F.; Sommer, R.L.; Durin, G.; Zapperi, S.S.; Setna, J.P. Universality beyond power laws and the average avalanche shape. *Nat. Phys.* **2011**, *7*, 316–320. [CrossRef]
18. Kamel, S.M.; Samy, N.M.; Tóth, L.Z.; Daróczi, L.; Beke, D.L. Denouement of the Energy-Amplitude and Size-Amplitude Enigma for Acoustic-Emission Investigations of Materials. *Materials* **2022**, *15*, 4556. [CrossRef]
19. Casals, B.; Dahmen, K.A.; Gou, B.; Rooke, S.; Salje, E.K.H. The duration-energy-size enigma for acoustic emission. *Sci. Rep.* **2021**, *11*, 5590. [CrossRef] [PubMed]

20. Spark, G.; Maas, R. Shapes and velocity relaxation of dislocation avalanches in Au and Nb microcrystals. *Acta Mater.* **2018**, *152*, 86–95. [CrossRef]
21. Planes, A.; Manosa, L.; Vives, E. Acoustic emission in martensitic transformations. *J. Alloys Compd.* **2013**, *577*, S699–S704. [CrossRef]
22. Dobrinevski, A.; Le Doussal, P.; Weise, K.J. Avalanche shape and exponents beyond mean-field theory. *Europhys. Lett.* **2015**, *108*, 66002. [CrossRef]
23. Vu, C.-C.; Weiss, J. Asymmetric Damage Avalanche Shape in Quasibrittle Materials and Subavalanche (Aftershock) Clusters. *Phys. Rev. Lett.* **2020**, *125*, 105502. [CrossRef]
24. Antonaglia, J.; Wright, W.J.; Gu, X.; Byer, R.R.; Hufnagel, T.C.; LeBlanc, M.; Uhl, J.T.; Dahmen, K.A. Bulk metallic glasses deform via avalanches. *Phys. Rev. Lett.* **2014**, *112*, 1555501. [CrossRef] [PubMed]
25. Tóth, L.Z.; Bronstein, E.; Daróczi, L.; Shilo, D.; Beke, D.L. Scaling of average avalanche shapes for acoustic emission during jerky motion of single twin boundary in single-crystalline Ni2MnGa. *Materials* **2023**, *16*, 2089. [CrossRef]
26. Kamel, S.M.; Daróczi, L.; Tóth, L.Z.; Panchenko, E.Y.; Chumlyakov, Y.I.; Samy, N.M.; Beke, D.L. Acoustic emission and DSC investigations of anomalous stress-stain curves and burst like shape recovery of Ni49Fe18Ga27Co6 shape memory single crystals. *Intermetallics* **2023**, *159*, 107932. [CrossRef]
27. Clauset, A.; Shalizi, C.R.; Newman, M.E. Power-Law Distributions in Empirical Data. *SIAM Rev.* **2009**, *51*, 661–703. [CrossRef]
28. Beke, D.L.; Bolgar, M.K.; Toth, L.Z.; Daroczi, L. On the asymmetry of the forward and reverse martensitic transformations in shape memory alloys. *J. Alloys Compd.* **2018**, *741*, 106–115. [CrossRef]
29. Otsuka, K.; Ren, X. Mechanism of martensite aging effects and new aspects. *Mater. Sci. Eng.* **2001**, *A312*, 207–218. [CrossRef]
30. Timofeeva, E.; Panchenko, E.Y.; Tokhmetova, A.B.; Eftifeeva, A.B.; Chumlyakov, Y.I.; Volochaev, M.N. The cyclic stability of rubber-like behaviour in stress-induced martensite aged Ni49Fe18Ga27Co6 (at.%) single crystals. *Mat. Lett.* **2021**, *300*, 130207. [CrossRef]
31. Li, J.; Zhang, J.-z.; Zeng, L.-y.; Wang, S.; Song, X.-y.; Chen, N.-l.; Zuo, X.-w.; Rong, Y.-h. Revealing dislocation activity modes 980 during yielding and uniform deformation of low-temperature tempered steel by acoustic emission. *J. Iron Steel Res. Int.* **2024**, *31*, 3022–3036. [CrossRef]
32. Zhao, Y.; Ding, X.; Sun, J.; Salje, E.K.H. Thermal and athermal crackling noise in ferroelastic nanaostuctures. *J. Phys. Condens Matter* **2014**, *26*, 142201. [CrossRef]
33. Nataf, G.; Salje, E.K.H. Avalanches in ferroelectric and coelastic materials: Phase transition, domain switching and propagation. *Feroelectrics* **2020**, *569*, 82–107. [CrossRef]
34. Zreihan, N.; Faran, E.; Vives, E.; Planes, A.; Shilo, D. Coexistence of a well-determined kinetic law and a scale-invariant power law during the same physical process. *Phys. Rev. B* **2018**, *97*, 014103. [CrossRef]
35. Zreihan, N.; Faran, E.; Vives, E.; Planes, A.; Shilo, D. Relations between stress drops and acoustic emission measured during mechanical loading. *Phys. Rev. Mater* **2019**, *3*, 043603. [CrossRef]
36. Daróczi, L.; Piros, E.; Tóth, L.Z.; Beke, D.L. Magnetic field induced random pulse trains of magnetic and acoustic noises in martensitic single-crystal Ni2MnGa. *Phys. Rev. B* **2016**, *96*, 014416. [CrossRef]
37. Chen, Y.; Gou, B.; Yuan, B.; Ding, X.; Sun, J.; Salje, E.K.H. Multiple Avalanche Processes in Acoustic Emission Spectroscopy: Multibranching of the Erenergy-Amplitude Scaling. *Phys. Stat. Sol. B* **2021**, *259*, 2100465. [CrossRef]
38. Chen, Y.; Gou, B.; Ding, X.; Sun, J.; Salje, E.K.H. Fine structure of acoustic emission spectra: How to separate dsiclocation movements and entanglements in 316L stainless steel. *Appl. Phy. Lett.* **2020**, *117*, 262901. [CrossRef]
39. Chen, Y.; Gou, B.; Ding, X.; Sun, J.; Salje, E.K.H. Real-time monitoring dislocations, martensitic transfromations and detwinning in stainless steel: Statistical analysis and mashine learning. *J. Mat. Sci Technol.* **2021**, *92*, 31–39. [CrossRef]
40. Chen, Y.; Gou, B.; Xu, X.; Ding, X.; Sun, J.; Salje, E.K.H. Multibranches of acoustic emission as identifier for deformation mechanisms in additively manufactured 316L stainless steel. *Addit. Manuf.* **2023**, *78*, 103819. [CrossRef]
41. McFaul, L.W.; Wright, W.J.; Sickle, J.; Dahmen, J.A. Force oscillations distort avalanche shapes. *Mater. Res. Lett.* **2019**, *7*, 456–502. [CrossRef]
42. Utsu, T.; Ogata, Y.; Matsu'ura, R.S. The Centenary of the Omori Formula for a Decay Law of Aftershock Activity. *J. Phys. Earth* **1995**, *43*, 1–33. [CrossRef]